Molecular understanding of charge storage and charging dynamics in supercapacitors with MOF electrodes and ionic liquid electrolytes

Molecular understanding of charge storage and charging dynamics in supercapacitors with MOF electrodes and ionic liquid electrolytes

Sheng Bi[1,2], Harish Banda[3], Ming Chen[1,4], Liang Niu[1], Mingyu Chen[1], Taizheng Wu[1], Jasheng Wang[1], Runxi Wang[1], Jiamao Feng[1], Tianyang Chen[3], Mircea Dincă[3], Alexei A. Kornyshev[2,*], and Guang Feng[1,*]

Abstract

We performed constant-potential molecular dynamics simulations to analyze the double layer structure and capacitive performance of supercapacitors composed of conductive metal−organic framework (MOF) electrodes and ionic liquids. The molecular modeling unravels how ions transport and reside inside polarized porous MOFs, and then predicts the corresponding potential-dependent capacitance in characteristic shapes. Transmission line model was adopted to characterize the charging dynamics, which further allowed evaluating the capacitive performance of this class of supercapacitors at macroscale from the simulation-obtained data at nanoscale. These 'computational microscopy' results were testified by macroscopic electrochemical measurements. Such combined nanoscale-to-macroscale investigation demonstrates the potential of MOF supercapacitors for achieving unprecedentedly high volumetric energy and power densities. It gives molecular insights into preferred structures of MOFs for accomplishing consistent performance with optimal energy–power balance, providing a blueprint for future characterization and design of these new supercapacitor systems.

[1]State Key Laboratory of Coal Combustion, School of Energy and Power Engineering, Huazhong University of Science and Technology (HUST), Wuhan 430074, China.
[2]Department of Chemistry, Faculty of Natural Sciences, Imperial College London, Molecular Sciences Research Hub, White City Campus, W12 0BZ, London, United Kingdom.
[3]Department of Chemistry, Massachusetts Institute of Technology, Cambridge, MA, 02139, United States.
[4]Shenzhen Research Institute of HUST, Shenzhen, 518057, China.
*e-mail: a.kornyshev@imperial.ac.uk; gfeng@hust.edu.cn

Enhancing capacitive performance of **e**lectrical **d**ouble **l**ayer **c**apacitors (EDLCs) relies on the development of porous electrode materials.[1, 2] Owing to their designable structures,[3, 4, 5] conductive **m**etal-**o**rganic **f**rameworks (MOFs) are promising for EDLC electrodes.[5, 6, 7, 8] Their scaffold-shaped volume-filling ordered structure could bring large **s**pecific **s**urface **a**rea (SSA) per mass/volume, with a custom-designed pore space.[3, 6] This helps to maximize the stored energy density; it may also facilitate ion transport, thereby increasing power density. Indeed, graphene-doped MOFs were found to give high capacitance, due to their high porosity and open structure.[9] Highly conductive Ni_3(2,3,6,7,10,11-hexaiminotriphenylene)$_2$ (Ni_3(HITP)$_2$) MOF-electrodes in EDLCs with an organic electrolyte showed high areal capacitance and low cell resistance, superior to most carbon-based materials.[10]

The choice of electrolyte is equally important. **R**oom **t**emperature **i**onic **l**iquids (RTILs) are promising electrolytes due to their excellent thermal stability, nonvolatility, broad working temperature range, and wide electrochemical window (potentially facilitating the EDLC's energy density).[11, 12, 13, 14] Many studies focused on understanding the energy-storage mechanism of porous electrodes with RTILs, via *in situ* experiments and molecular simulations.[11, 15, 16, 17, 18] Traditional electrodes, e.g. activated carbons, contain pores of different sizes, shapes, and connectivities,[1, 2, 3] whereas MOFs present monodisperse pores of controllable structures,[3, 4, 5, 7] making them near-ideal systems for computational modeling. Nevertheless, because there could be millions of MOF-RTIL combinations, it is important to unravel generic charge-storage mechanisms and charging dynamics related to their structures, particularly in the absence of experimental studies on supercapacitors with conductive MOF-electrodes and RTIL-electrolytes.

Herein, we focus on this task, using 'computational microscopy': **m**olecular **d**ynamics (MD) simulations based on atomistic models of MOFs and coarse-grained models of RTILs and connecting with 'experimental macroscopy': electrochemical measurements on MOF-RTIL supercapacitors. Fig. 1a shows our MD setup; we consider three types of electrodes based on densely stacked 2D-conductive MOF-sheets with different-sized quasi-1D pores (Fig. 1b-c), and 1-ethyl-3-methylimidazolium tetrafluoroborate ([EMIM][BF_4]) as the electrolyte (Fig. 1d). In simulations, we control the voltage between cathode and anode by constant potential method. Details see Methods and Supplementary Parts 1-2. After equilibrating the system at the **p**otentials of **z**ero **c**harge (PZC), we apply jump-wise voltages between two electrodes, and then

monitor the follow-up charging dynamics and charge/ion distributions. We explore structures of ionic distributions in electrically polarized nanoscale pores, and the options for energy storage and power delivery that these structures proffer. Finally, we experimentally test the simulation-predicted performance.

Equilibrium charge and ion distributions inside MOFs

We present the simulated charge and ion distributions in three neutral and polarized MOFs in pore sizes of 0.81, 1.57 and 2.39 nm, with PZC calculated as 0.074, 0.035 and 0.042 V, respectively. The small PZC values suggest that no noticeable preferential adsorption of cations or anions of [EMIM][BF_4] into the pores of these MOFs.[19]

Figure 2a depicts the in-plane distributions in a 1.57-nm-diameter pore at different electrode potentials. Inside quasi-1D pores of a polarized MOF-electrode, radial ion distributions appear more heterogeneous than those at PZC, with counter-charge settling closer to the pore surface and at pore center-line (up row of Fig. 2a). At PZC, as shown in the middle and bottom rows of Fig. 2a, cations and anions both form a layer adsorbed on the pore surface, displaying a hexagonal pattern in the planar-cross-section, with a wire of ions along the pore axis. Under electrode polarization, the *counter-ions* (cations at negative and anions at positive polarization) pack similarly but with more distinct separation between a surface-adsorbed layer and the center-line. The *co-ions* settle between these two regions. For the smallest pore MOF (0.81 nm), only one layer of ions can get inside the pore, regardless of electrode polarization (Supplementary Figure 5). For the largest pore (2.39 nm), at PZC, two mixed cation-anion layers dwell inside the pore, one of them contacting pore wall; with electrode polarization two pronounced counter-ion layers form separated by a co-ion layer, with a co-ion wire at the axis (Supplementary Figure 6).

The interlaced radial distributions of cations and anions in polarized pores comply with the ion layering in RTILs at electrode surfaces revealed by previous experiments and simulations,[11, 15, 16, 17] while there is little cation-anion layering at PZC (middle column of Fig. 2a). To delve into this difference, we analyzed the ion density along the pore axis. In Supplementary Figure 7a we see waving axial ion distributions at PZC become more distinct with electrode polarization. Examining ions inside pores, we divided the pore space into central and surface regions demarcated by a circle (Fig. 2b and snapshots in Supplementary Figure 7b). The cation orientations, characterized by angular distributions (Fig. 2c), reveal how ions get accommodated

inside the pore. As the electrode gets more negatively charged, cations in the surface region prefer to align along the pore axis, while those in the central region orient more randomly, which could be ascribed to the adsorbed ion layer screening out the electrode surface charge. With positive polarization, the cations move closer to the center-axis and leave their ethyl groups pointing to surface-adsorbed anions. Similar trends could be observed for smaller and larger pores (Supplementary Figures 8 and 9), except that ions in the central region of larger pores orientate more randomly. The delineated in-plane and axial ion distributions unravel where and why ions could preferably reside in MOF-pores.[11, 15, 20]

Capacitance and energy density of MOF-based supercapacitors

Charge storage in supercapacitors is characterized by voltage-dependent capacitance and energy density. Differential capacitance of an electrode is defined as the derivative of the electrode's charge with respect to its potential (Methods and Supplementary Part 2). The electrode charge is equal with an opposite sign to the net ionic charge inside the pores and in the double layer at the electrode's outer surface. For highly porous electrodes, the area of the latter is negligible, and we will not consider that contribution.

The capacitance is usually presented per unit (i) surface area (*area-specific*), (ii) mass (*gravimetric*), or (iii) volume (*volumetric*) of the electrode. The gravimetric and volumetric values are easy to define, whereas the determination of the area-specific capacitance could be ambiguous, as it depends how the interior surface of the electrode was measured (the way how we estimated 'surface area' of the studied MOF-pores is described in Supplementary Part 1). Fig. 3a shows the area-specific differential capacitance. The MOF with the smallest pore (0.81 nm) displays a camel-like shape of the capacitance-potential curve with two maxima of 10.2 and 8.8 μF cm^{-2} at -1.1 and +1.5 V, respectively, while the curves for the other two MOFs are both bell-shaped with a maximum near PZC. Within a potential range of -0.5 to +0.5 V, the 1.57-nm-diameter MOF delivers a capacitance of ~9 μF cm^{-2}, compatible with RTIL-based porous carbon EDLCs.[17, 21] The shape of the capacitance-potential curves could be understood through analyzing the voltage-dependent ion distributions inside pores (Supplementary Figure 10). There, for the smallest pore MOF, the number of in-pore cations and anions, separately, gradually changes within the potential range between -1 and +1.4 V (Supplementary Figure 10a). The change gets faster under larger electrode polarizations, slowing down after ±2 V, approaching

saturation. This results in the camel-like shape of capacitance-potential curve (Fig. 3a). For the other two MOFs (Supplementary Figure 10b-c), the steepest change in ion population occurs near PZC, slowing down as electrodes get more polarized (especially, over ±1.5 V); this induces bell-shaped capacitance-potential curves (Fig. 3a). Notably, for pores filled with more than one ion layer, within the potential range of -0.5 to +0.5 V the change of cation/anion population takes place majorly in the central region of a pore, but it shifts towards the pore surface region beyond this range (Supplementary Figure 10d-e).

Having defined the mass and volume of a unit cell for the studied MOFs, we obtain the gravimetric/volumetric capacitances, and the corresponding energy densities. As shown in Fig. 3b-c, the MOF with the largest pore (2.39 nm) has the highest gravimetric capacitance but lowest volumetric one. For 1.57-nm MOF $Ni_3(HHB)_2$, the gravimetric and volumetric capacitances reach 112 F g^{-1} and 105 F cm^{-3}, respectively. Noteworthy, simulations show that a gravimetric energy density of ~57 Wh kg^{-1} could be achieved at a cell voltage of 4 V, if the electrodes could sustain this voltage. Such energy density is as high as those reported for some high-energy-density carbon electrodes.[22] With regards to volumetric energy density, especially within a narrower potential range, three MOF electrodes display similar capacitances, while at 4 V, the smallest pore MOF delivers the highest volumetric energy density, ~50 Wh L^{-1}. The predicted volumetric performance demonstrates promising potential of these MOFs in comparison with other electrode materials in EDLCs.[23, 24]

Certainly, as the pore size of MOFs keeps reducing, ions eventually will not be able to enter the pores, leading to vanishing capacitance. Indeed, MOF Ni_3(hexaaminobenzene)$_2$ ($Ni_3(HAB)_2$),[8] with quite less room than $Ni_3(HHB)_2$ to accommodate enough ions inside, was explored to exhibit considerably smaller capacitance, suggesting that there would be a limit of narrowing MOF pore for a typical RTIL (Supplementary Part 4).

Charging dynamics

We focus now on power delivery. Figure 4a shows the time evolution of ionic charge in a pore at 400 K (for results between 300 to 400 K, see Supplementary Figure 13). It appears possible to rationalize the charging dynamics through the **t**ransmission **l**ine **m**odel (TLM).[25] Based on TLM schematized in Supplementary Figure 14a, the net charge of the pore, after jump-wise applying a constant potential, reads:[25]

$$Q(t) = Q_\infty \left\{ 1 - \frac{2}{\pi^2} \sum_{n=0}^{\infty} \frac{\exp\left[-\pi^2 \left(n+\frac{1}{2}\right)^2 \left(\frac{2l}{L}\right)^2 \frac{t}{\tau}\right]}{\left(n+\frac{1}{2}\right)^2} \right\} \quad (1)$$

where Q_∞ is the charge when the pore gets fully charged, l is the pore volume divided by its surface area, and L is the full length of the pore. The parameter in Eq. (1), which does not depend on pore length, is the intrinsic relaxation time,

$$\tau = \frac{C_{area} \times l}{\sigma} \quad (2)$$

in which C_{area} is the areal capacitance of the pore and σ is the ionic conductivity inside the pore. Note that Eq. (1) is strictly valid for potential-independent capacitance; there is no closed-form solution if the capacitance varies during charging. For simplicity, we will still use Eqs. (1) and (2) with the value of C_{area} corresponding to the capacitance for a given electrode potential.

Taking 1.57-nm-diameter MOF, with l = 0.40 nm and L = 5.86 nm (parameters for the other two MOFs, see Supplementary Tables 2-3), by fitting TLM to simulation data we obtain τ. Despite the aforementioned approximation, TLM-fitted curves match the MD-obtained charging curves very well (see Fig. 4a). This is further confirmed by fittings of the charging dynamics under alternative voltage-jumps and at different temperatures (Supplementary Figures 13 and 14b-d). The fittings for all three studied MOFs show that with increasing temperature, τ decreases (top panel of Fig. 4b), which is reasonable and has been experimentally demonstrated for porous electrodes owing to the increase of ion mobility with temperatures[26, 27]. The obtained value of τ can be used to roughly estimate the charging time, $\tau_0 = \frac{\tau}{(l/L)^2}$, for a practical supercapacitor cell. For instance, for 1.57-nm-pore MOF-electrode of 100 μm thickness, τ_0 will be 4.3 and 2.2 seconds at 300 and 400 K, respectively.

Specially performed MD-simulations of bulk [EMIM][BF_4] give conductivity of 1.26-8.2 S m^{-1} within 300-400 K, consistent with experimental data (1.6-10.8 S m^{-1}).[28] To evaluate the conductivity of in-pore RTIL, we extracted the values of τ from fitting Eq. (1) to the MD-obtained charging curves of Fig. 4a, and then get σ, using Eq. (2). For MOFs with pore sizes of 1.57 and 2.39 nm, σ increases from 0.3-0.9 S m^{-1} within 300-400 K (bottom panel of Fig. 4b). Interestingly, the conductivity of ions in the smallest pore (0.81 nm), varying within 0.9-1.7 S m^{-1} in such temperature interval, appears higher than in the other two larger MOF pores. This could be attributed to the stronger screening electrostatic interactions due to the induced image charges

on the pore walls.[29, 30] Nevertheless, the conductivities of ions under nanoconfinements are obviously smaller than in the bulk.

These results suggest considerable limitations for ion transport inside the quasi-1D MOF-pores. Hence, the electrolyte resistance in MOFs would be the dominant contribution to the equivalent series resistance (ESR) of a practical MOF-based EDLC. This is similar to what has been concluded from the experiment with 1.57-nm-pore MOF in an organic solution.[10] It is simply because that the electrical conductivity of this MOF is much higher than the ionic conductivity of RTIL. Interestingly, the larger working voltage results in a decrease of τ and an increase of σ (Supplementary Figure 14e-g), thus promoting faster ion transport inside MOFs.

All the above simulations are conducted with RTIL in coarse-grained model[31] and MOF-electrode in AA interlayer stacking.[32] To verify the independence of the model on results, we employed an all-atom model for [EMIM][BF_4] (Supplementary Figure 15).[33] All-atom model gave results very similar to the coarse-grained one, including in-pore ion distributions, charge storage and charging dynamics (Supplementary Figures 16-18). To reveal the effect of interlayer stacking, we performed MD simulations on a slipped-parallel AB stacking model[32] of MOF $Ni_3(HITP)_2$ (Supplementary Figure 19a). The tiny parallel slip (0.137 nm) introduces a negligible difference in both capacitance and charging dynamics (Supplementary Figure 19b).

Capacitive performance at macroscale

To validate MD-obtained capacitance, we, taking MOF $Ni_3(HITP)_2$ as an example, carried out electrochemical measurements of supercapacitors with [EMIM][BF_4] electrolyte. We have set three synthesis procedures (see Methods), based on previously reported strategies,[10, 34] and obtained $Ni_3(HITP)_2$ samples with SSAs of 556, 641 and 732 $m^2 g^{-1}$ (Supplementary Figure 20). Scanning electron micrographs demonstrate that the sample with higher SSA has larger rob-like crystallite in the MOF powder (Supplementary Figure 21), indicating enhanced crystallinity,[8, 35, 36] as verified by the powder X-ray diffraction patterns of the samples with different SSA (Supplementary Figure 22).

Two-electrode cells were fabricated, with these $Ni_3(HITP)_2$ samples of different crystallinity, to measure the capacitance of this MOF in RTIL [EMIM][BF_4] (for details see Methods). With cyclic voltammogram (CV) measurements at a scan rate of 10 mV s^{-1} (Fig. 5a, for results at 5

mV s^{-1} see Supplementary Figure 23), we obtained that the gravimetric capacitances for $Ni_3(HITP)_2$, with SSAs of 556, 641 and 732 m^2 g^{-1}, are, respectively, 58, 70 and 76 F g^{-1}, which are all smaller than the MD-obtained capacitance of ~101 F g^{-1} with SSA of 1153 m^2 g^{-1}. This difference could be ascribed to the different SSAs resulting from the imperfect crystallinity (Supplementary Figures 21-22). The areal capacitance, however, depends little on the SSA (~11 μF cm^{-2}, Supplementary Table 5), and is close to the modeling value of ~9 μF cm^{-2}. This weak crystallinity-dependent areal capacitance of MOF-electrode suggests that pores accessible to ions contribute equally to charge storage, which is essentially different from typical porous carbons with pores of different size and shape. Accordingly, by improving the MOF crystallinity, one could achieve both larger SSA and higher gravimetric capacitance, closer to the modeling value.

The up-to-date conductive MOFs, however, have smaller electrochemical voltage windows (limited by the onset of electrochemical reactions under positive and negative polarizations) than those achieved for metallic electrodes with RTILs.[5, 6, 7, 8, 10, 13, 14] Our CV measurements of $Ni_3(HITP)_2$ in a three-electrode cell indicate that enhancing MOF crystallinity, accompanied with SSA increase from 556 to 732 m^2 g^{-1}, would also enlarge its voltage window from about 2.1 to 2.8 V (Supplementary Figure 24). Our cycle-life tests further confirm the increased working voltage with improving crystallinity, although the voltage window shrinks a little (Supplementary Figure 25).

We then measured the ESR of MOF-based EDLCs. The galvanostatic charge-discharge (GCD) curve in Fig. 5b was experimentally obtained at room temperature for two-electrode cells composed of 25 μm separator and MOF $Ni_3(HITP)_2$ pellets with 180 μm thickness and 6.4 mm diameter. Then, the ESR was found to be 8.6 Ω cm^2, similar to our electrochemical impedance spectroscopy (EIS) data (8.9 Ω cm^2, Supplementary Figure 27). Previous experiments have reported a smaller ESR of this MOF than of porous carbons in organic electrolyte.[10] To identify this advantage of $Ni_3(HITP)_2$ in RTIL electrolyte, a commercial activated carbon (YP-50F) was chosen for comparison, with nearly the same size and mass loading and without any binders and additives. The ESR for the assembled cells with [EMIM][BF_4] was determined from GCD curves as about 7.2 and 15.9 Ω cm^2, respectively, for electrodes made of $Ni_3(HITP)_2$ and activated carbon with Ni foam collectors (Supplementary Figure 26). It was earlier experimentally demonstrated that the electrodes based on aligned single-walled carbon

nanotubes show greatly enhanced ion transport parallel to the alignment direction.[37] Similarly, the MOFs studied herein, possessing crystal structure and retaining crystallinity when made into electrodes,[10, 32] could offer straight quasi-cylindrical pores, providing faster charging dynamics than the carbon with tortuous pores and amorphous topology.

The MD-obtained capacitance and conductivity of electrolyte in a MOF pore, together with intrinsic properties of MOFs (Supplementary Table 2), could be used to assess the capacitive performance of a 'practical' MOF-based supercapacitor, via macroscale equivalent circuit simulations (for details see Methods and Supplementary Part 7). Based on the values of σ and capacitance, for three studied MOFs, Nyquist plots were computed for supercapacitors with the same sized MOF-electrode (180 μm thickness and 6.4 mm diameter) and separator (25 μm thickness). They differ, to some extent, from EIS measurement (Fig. 6a vs. Supplementary Figure 27), as modeling adopts ideal monocrystalline MOF electrodes and neglects the electrode and electrode-collector contact resistances. From simulation-obtained Nyquist plots, ESRs of such cells at 400 K were obtained as 3.1, 2.9 and 2.3 Ω cm^2 for MOFs with the pore size of 0.81, 1.57 and 2.39 nm, respectively. At 300 K, ESR increases to approximately 6.4 Ω cm^2 for three MOF electrodes (Fig. 6b), which is compatible with our experimental values from both GCD and EIS measurements. These results indicate that the ESR of MOF-electrode EDLCs is dominated by the resistances of the in-pore electrolytes. Therefore, molecular modeling is a quite appropriate approach to assessing both charge storage and charging dynamics of MOF supercapacitor at macroscale.

Ragone plots for temperature-dependent power-energy relationships are shown in Fig. 6b-c. The temperature has minor influence on maximal energy density but has a large effect on the power density. For applications demanding the best gravimetric performance, MOFs with the largest pore size (2.39 nm) seem to be a better choice, delivering both higher energy and power density, in comparison with the other two MOFs (Fig. 6b). As the temperature increases from 300 to 400 K, under a cell voltage of 2.8 V, the MOF with the largest pore size could reach power density of 20-46 kW kg^{-1} and an energy density about 30 Wh kg^{-1}. For optimized volumetric performance, all three MOFs exhibit similar promising performance, with a power density range of 13-30 kW L^{-1} and energy density of ~20 Wh L^{-1}. These compare favorably with performance of most reported carbon-based EDLCs (Supplementary Table 6).[22, 23, 24, 38, 39] As

expected, under higher voltages, the energy and power densities would both increase (Supplementary Figure 29).

Conclusion

We have investigated the charge storage and charging dynamics of supercapacitors consisting of conductive MOF electrodes and RTIL electrolyte. The microstructures of RTIL inside MOF pores were analyzed in terms of in-plane (2D) and axial (1D) ion distributions, as well as ion orientations, which help interpret the obtained camel- and bell-shapes of the capacitance-potential dependence. With TML rationalizing the charging dynamics, we evaluated the capacitive performance of macroscale EDLC devices. Modeling results revealed that these MOF/RTIL-based cells could exhibit performance superior to most carbon-based devices,[22, 23, 24, 38, 39] which suggest promising avenues for designing supercapacitors with both high energy and power densities.

The improvement of MOF crystallinity obtained through different synthesis procedures was shown to enlarge not only their SSA and particle size[8, 35, 36] but also their working voltage. The electrochemical measurements on supercapacitors made of MOF materials solely as electrodes and RTILs as electrolytes have shown that the gravimetric capacitance increases with SSA. The ESR of MOF is quite smaller than similarly structured cell with a typical commercial porous carbon, showing the benefit of the well-controlled monodisperse pore structures in MOFs. Both areal capacitance and resistance obtained in experiment agree with modeling, signifying that our molecular simulation could well represent the real system of MOF-based supercapacitor.

Although many conductive MOFs have been synthesized,[5, 6, 7, 8, 40] they are still a new family in MOF community and more of them require to be developed, which would take the modeling-guided design as key input. Moreover, to be developed 3D conductive MOFs scaffolds might be expected to have advantages over the dense stacks of 2D-MOF-sheets with quasi-1D pores. Indeed, 3D scaffolds could provide ion transport paths in all directions and consequently promote cation-anion swapping, pivotal in charging-discharging processes. Such scaffold-electrodes with the all-dimension openness and high porosity may help enhance the charging dynamics, and together with the enhanced surface area, potentially enlarge energy and power densities simultaneously.

Methods

Molecular dynamics simulation

As shown in Fig. 1, the MD simulation system consists of two identical and symmetric conductive MOFs immersed in a RTIL [EMIM][BF_4]. Real supercapacitors certainly contain an electronically isolating ion transport membrane that warrants the absence of a short-cut between the electrodes, however, ideal membranes must not impede ion exchange between the electrodes. For this proof-of-the principle study, considering therefore the best performance possible, we will not incorporate the membrane into our simulation cell. This strategy is generally adopted for MD modeling of supercapacitors.[15, 17, 25, 31, 41] The atomistic structures of MOF $Ni_3(HITP)_2$ were obtained from experimental measurements,[32] and MOFs Ni_3(hexahydroxybenzene)$_2$ ($Ni_3(HHB)_2$) and Ni_3(2,3,8,9,14,15-hexaiminotrinaph thalene)$_2$ ($Ni_3(HITN)_2$) were constructed, respectively, with reference to $Cu_3(HHB)_2$ (Ref. [42]) and $Ni_3(HITP)_2$. The geometry optimization of each MOF in Fig. 1c and the partial charge distribution for each MOF in unpolarized state (Supplementary Figure 1) were derived from DFT calculations, using in Vienna ab initio simulation package (VASP)[43]. Furthermore, the corresponding density of states was computed to demonstrate that all the MOFs studied are conductive (Supplementary Figure 2), though $Ni_3(HHB)_2$ and $Ni_3(HITN)_2$ have yet been successfully synthesized. Details of MOF structure optimization of MOFs and pore size calculation can be seen in Supplementary Part 1 and Supplementary Tables 1-2. The Lennard-Jones parameters for the MOF atoms were taken from the generic universal force field (UFF)[44]; the coarse-grained model was adopted for [EMIM][BF_4], which could provide the proper thermodynamic and dynamic properties[31]. The simulation cells were chosen as large enough to reproduce the bulk state in the central region of RTIL reservoir connected with two electrodes, and periodic boundary conditions were applied in all directions. Specific system parameters are given in Supplementary Table 3.

Simulations were performed in the NVT ensemble using a customized MD software GROMACS.[45] The applied electrical potential between the two electrodes in Fig. 1 was maintained by the constant potential method (CPM), as it allows the fluctuations of charges on electrode atoms during the simulation.[15, 31, 41] Details of CPM could be found in Supplementary Part 2. To guarantee the accuracy, the electrode charges are updated on the fly of simulation running at every simulation step (2 fs). The electrolyte temperature was maintained at 400 K

using the V-rescale thermostat[46]. The electrostatic interactions were computed using the particle mesh Ewald method[47]. An FFT grid spacing of 0.1 nm and cubic interpolation for charge distribution were used to compute the electrostatic interactions in the reciprocal space. A cutoff length of 1.2 nm was used in the direct summation of the non-electrostatic interactions and electrostatic interactions in the real space. For each conductive MOF, the MD system was annealed from 500 to 400 K over a period of 10 ns, following by running another 40 ns to reach equilibrium under null electrode potential. To explore the charging dynamics, five independent runs were performed for smoothing the charging process data. To obtain microstructure and capacitance, a simulation was performed for 60 ns to surely reach equilibrium under the applied potential ranging from 0 to 6 V, and then another 60 ns production in equilibrium state was run for analysis.

In metallic electrodes, before the onset of electrochemical reactions, there are no limitations on accommodating or depleting electrons. Their capacitance is determined by their ability to accumulate the ionic charge from electrolyte. In electrodes built from low dimensional materials, such as graphene and its derivatives, accommodation of electrons has its own laws that give rise to the **q**uantum **c**apacitance (QC) contribution;[48, 49, 50] when the electrode's QC is much larger than the electrolytic capacitance, the total capacitance will be predominated by the ionic contribution.[16, 50] Thick dense stacks of 2D MOF sheets, even those that deliver large pores are not electronically low-dimensional. Unless concentration of charge carriers in them is as low as in wide-band-gap semiconductors, they are expected to perform like bulk porous metallic electrodes; our density function theory (DFT) calculations demonstrate that all MOFs studied here are well conductive (Supplementary Figure 2); thus we focus on the ionic contribution.

Therefore, the electrode potential was obtained as the potential difference between the electrode and the electrolyte reservoir and calibrated relative to PZC of the electrode, and then the differential capacitance was calculated by taking derivatives of the MD-obtained surface charge density as a function of electrode potential (details can be seen in Supplementary Part 2 and Supplementary Figure 4). The electrical conductivity of the bulk [EMIM][BF_4] was evaluated via the time integral of ECACFs, $\sigma_{RTIL} = \frac{1}{3Vk_BT}\int_0^\infty < \vec{J}(0) \cdot \vec{J}(t) > dt$, in which V is the system volume and $\vec{J}(t)$ denotes the electrical current. $\vec{J}(t)$ is defined by $\vec{J} = \sum_{i=1}^{N} q_i \vec{v}_i$, where N is the total number of ions, and q_i and $\vec{v}_i(t)$ are the charge and velocity of the i-th ion,

respectively.

It is worth noting that static prosperities of EDLCs were studied at a temperature of 400 K that is generally used for MD simulations to get the ion structure and capacitance[25, 31], while the charging dynamics was ascertained within a temperature range of 300-400 K due to the big impact of temperature on dynamic properties[26, 27].

Equivalent electrical circuit simulation

We conceived a practical size two-electrode symmetric cell (see Supplementary Figure 28a), based on our EDLC cell with $Ni_3(HITP)_2$ pellet electrodes in experiment. Specifically, the diameter of the MOF electrode was set as 6.4 mm, and the electrode thickness was taken as 180 μm for three studied MOFs in Fig. 1. The equivalent circuit model of the conceived two-electrode symmetric cell was based on RC transmission line circuit in which the resistors and the capacitors were calculated based on the size of the cell and the MD-obtained specific capacitance and conductivity of ions in MOF. The circuit simulations were performed via *Simulink*, in which impedance measurement and constant power load (via boosting DC-DC converter block) tests were carried out respectively to obtain the Nyquist plots and Ragone plots for three MOF-based EDLCs in practical cell size. Detail can be seen in Supplementary Part 8 with Supplementary Figure 28.

Materials for experiments

All the starting materials were purchased from commercial suppliers. Specifically, 2,3,6,7,10,11-hexaaminotriphenylene hexahydrochloride (HATP·6HCl) was purchased from Alfa; $NiCl_2 \cdot 6H_2O$ was purchased from Sigma-Aldrich; Concentrated aqueous ammonia was purchased from TCI; Ethanol and acetone were purchased from Sinopharm. RTIL [EMIM][BF_4] was purchased from Aladdin. Starting materials were used without further purification unless otherwise noted. Activated carbon was purchased from Kurary Chemical, taken to compare with MOF electrode material.

Synthesis of MOFs

Based on synthesis strategies reported in the previous work,[10, 34] we obtained electrode materials of $Ni_3(HITP)_2$ with different surface areas of 556, 641, and 732 $m^2\ g^{-1}$, through three different

procedures which are given below.

Procedure I: A solution of 323 mg (1.36 mmol) of $NiCl_2 \cdot 6H_2O$ in 20 ml of water was added to a solution of 487 mg (0.91 mmol) of HATP·6HCl in 140 ml of water. Through this work, all the water used was deionized. Then 4.5 ml of concentrated aqueous ammonia (NH_4OH, 14.79 mol l^{-1}) was added to the mixture. The mixture was stirred in a flask under air bubbling for 1 h at 60 □, then air bubbling was turned off and the mixture was stirred for an additional 2 h at 60□. The resulting black powder was isolated by centrifugation immediately and washed with water (2 times, 180 ml) and ethanol (2 times, 180 ml). The solid was then dried under vacuum for 12 h at 150°C. The product was kept in refrigerator.

Procedure II: A solution of 162.1 mg (0.675 mmol) of $NiCl_2 \cdot 6H_2O$ in 10 ml of water was added to a solution of 243.7 mg (0.453 mmol) of HATP·6HCl in 70 ml of water. Then 2.25 ml of NH_4OH (14 mol l^{-1}) was added to the mixture. The mixture was stirred in a flask under air bubbling for 1 h at 60□, then air bubbling was turned off and the mixture was stirred for an additional 2 h at 60□. The resulting suspension was cooled in air for 1.5 h. The resulting black powder was isolated by centrifugation and washed with water (2 times, 90 ml) and ethanol (2 times, 90 ml). The solid was then dried under vacuum for 8 h at 100°C. After cooling, it was dried under vacuum for an additional 12 h at 100 °C. The product was kept in an argon-filled glovebox.

Procedure III: A solution of 96.5 mg (0.406 mmol) of $NiCl_2 \cdot 6H_2O$ in 10 ml of water was added to a solution of 142.0 mg (0.264 mmol) of HATP·6HCl in 50 ml of water in a 250-ml Schlenk bottle. The resulting yellow solution was stirred manually, heated to 65□ in an oil bath and treated with 1.5 ml of NH_4OH (14.79 mol l^{-1}). The reaction mixture was kept at 65□ for 45 min under continuous air bubbling upon which the reaction was switched to an N_2 atmosphere and kept at 65°C for an additional 2 h. The resulting suspension was cooled in an N_2 atmosphere for 2 h. The resulting black powder was separated from the reaction mixture by centrifugation, soaked in water at room temperature for 18 h, and washed with water (2 times,180 ml) , ethanol (2 times, 180 ml) and acetone (2 times, 180ml). Finally the solid product was dried under a stream of nitrogen gas for 12 h. The product was kept in an argon-filled glovebox.

Characterization of MOF powder

Nitrogen adsorption/desorption isotherms were measured with a Quantachrome Autosorb IQ system at 77 K. Before the gas adsorption/desorption measurement, as-synthesized MOFs (~100 mg) samples were activated by drying under vacuum for 12 h at 100 °C. Afterwards, liquid nitrogen baths (77 K) were used to measure nitrogen adsorption/desorption isotherms. The free space correction and measurement were conducted using ultrahigh-purity grade (99.999% purity) nitrogen and helium, oil-free valves, and gas regulators. Powder X-ray direction (PXRD) patterns were carried out with a PANalytical Empyrean X-ray Powder diffractometer equipped with a Cu-sealed tube (λ = 1.544426 Å) at 40 kV and 40 mA, and samples were prepared on a zero-background silicon crystal plate. Scanning electron microscopy (SEM) observation was performed with a Zeiss Gemini 300 SEM with an operating voltage of 3 kV. Transmission electron microscopy (TEM) was performed on a FEI Tecnai G2 F20 microscope and operated at 300 kV (point resolution 80 pm). Samples for TEM were dispersed in acetone, and a droplet of the suspension was transferred onto a carbon coated copper grid.

Electrochemical measurement and analysis of MOF electrodes

A two-electrode cell was fabricated to measure the capacitive performance of MOF electrodes in an Argonne-filled glovebox. Prior to electrochemical measurement, electrolyte [EMIM][BF_4] was vacuum-dried for 12 hours at 100 °C and then was treated with ultrapure argon (99.999%) to remove absorbed water and dissolved gas as much as possible. The cell is assumed to be symmetric, since the difference of MOF materials in two electrodes was controlled within 5%. All electrochemical measurements were performed on a Zahner Zennium electrochemical workstation.

Through this work, all the MOF electrodes were fabricated without any binders or conductive additives. To measure the capacitance, MOF powders were compressed into a Ni foam working electrode with a mass loading of ~4 mg cm^{-2}. We calculated the gravimetric capacitance (C_g) of one single electrode from the cyclic voltammetry curves, according to the following equation:

$$C_g = 4\frac{\int_0^{V_0/v} Idt}{V_0 m} \quad (3)$$

where I and v are the discharge current and the scan rate, respectively, V_0 is the operating voltage, and m is the total active material mass of both electrodes in the symmetric cell.

The experimental gravimetric capacitance (C_g) can be compared with MD-obtained integral capacitance (C_g^{MD}). C_g^{MD} can be obtained directly from the CPM simulation that is performed under V_0 potential drop between the two electrodes, as $C_g^{MD} = 4\frac{Q}{V_0 m}$, in which Q is the total charge on one electrode. To obtain the ESR, the electrode made of MOF pellets in 6.4 mm diameter and 180 μm thickness (mass loading ~5.9 mg cm^{-2}) on a 25-μm-thick Au foil. Through galvanostatic charge-discharge measurements, we computed the ESR from the voltage drop (V_{drop}) at the beginning of the discharge curve by ESR(Ω) = ($V_{drop}/2I$), where I is the constant discharge current.

References

1. Simon P, Gogotsi Y. Materials for electrochemical capacitors. *Nature Materials* 2008, **7**(11)**:** 845-854.
2. Sun H, Zhu J, Baumann D, Peng L, Xu Y, Shakir I*, et al.* Hierarchical 3D electrodes for electrochemical energy storage. *Nature Reviews Materials* 2018, **4:** 45-60.
3. Furukawa H, Cordova KE, O'Keeffe M, Yaghi OM. The Chemistry and Applications of Metal-Organic Frameworks. *Science* 2013, **341**(6149)**:** 1230444.
4. Guan BY, Yu XY, Wu HB, Lou XW. Complex Nanostructures from Materials based on Metal–Organic Frameworks for Electrochemical Energy Storage and Conversion. *Advanced Materials* 2017, **29**(47)**:** 1703614.
5. Wang H, Zhu Q-L, Zou R, Xu Q. Metal-Organic Frameworks for Energy Applications. *Chem* 2017, **2**(1)**:** 52-80.
6. Sun L, Campbell MG, Dincă M. Electrically Conductive Porous Metal–Organic Frameworks. *Angewandte Chemie International Edition* 2016, **55**(11)**:** 3566-3579.
7. Zhou J, Wang B. Emerging crystalline porous materials as a multifunctional platform for electrochemical energy storage. *Chemical Society Reviews* 2017, **46**(22)**:** 6927-6945.
8. Feng D, Lei T, Lukatskaya MR, Park J, Huang Z, Lee M*, et al.* Robust and conductive two-dimensional metal−organic frameworks with exceptionally high volumetric and areal capacitance. *Nature Energy* 2018, **3**(1)**:** 30-36.
9. Choi KM, Jeong HM, Park JH, Zhang Y-B, Kang JK, Yaghi OM. Supercapacitors of Nanocrystalline Metal–Organic Frameworks. *ACS Nano* 2014, **8**(7)**:** 7451-7457.
10. Sheberla D, Bachman JC, Elias JS, Sun C-J, Shao-Horn Y, Dincă M. Conductive MOF electrodes for stable supercapacitors with high areal capacitance. *Nature Materials* 2017, **16**(2)**:** 220-224.
11. Fedorov MV, Kornyshev AA. Ionic Liquids at Electrified Interfaces. *Chemical Reviews* 2014, **114**(5)**:** 2978-3036.
12. Hayes R, Warr GG, Atkin R. Structure and Nanostructure in Ionic Liquids. *Chemical Reviews* 2015, **115**(13)**:** 6357-6426.
13. Watanabe M, Thomas ML, Zhang S, Ueno K, Yasuda T, Dokko K. Application of Ionic Liquids to Energy Storage and Conversion Materials and Devices. *Chemical Reviews* 2017, **117** (10)**:** 7190-7239.
14. Armand M, Endres F, MacFarlane DR, Ohno H, Scrosati B. Ionic-liquid materials for the electrochemical challenges of the future. *Nature Materials* 2009, **8**(8)**:** 621-629.
15. Salanne M, Rotenberg B, Naoi K, Kaneko K, Taberna PL, Grey CP*, et al.* Efficient storage mechanisms for building better supercapacitors. *Nature Energy* 2016, **1:** 16070.
16. Vatamanu J, Borodin O, Olguin M, Yushin G, Bedrov D. Charge storage at the nanoscale: understanding the trends from the molecular scale perspective. *Journal of Materials Chemistry A* 2017, **5**(40)**:** 21049-21076.

17. Zhan C, Lian C, Zhang Y, Thompson Matthew W, Xie Y, Wu J*, et al.* Computational Insights into Materials and Interfaces for Capacitive Energy Storage. *Advanced Science* 2017, **4**(7)**:** 1700059.

18. Shao Y, El-Kady MF, Sun J, Li Y, Zhang Q, Zhu M*, et al.* Design and Mechanisms of Asymmetric Supercapacitors. *Chemical Reviews* 2018, **118**(18)**:** 9233-9280.

19. Vatamanu J, Borodin O, Smith GD. Molecular insights into the potential and temperature dependences of the differential capacitance of a room-temperature ionic liquid at graphite electrodes. *Journal of the American Chemical Society* 2010, **132**(42)**:** 14825-14833.

20. Kornyshev AA, Qiao R. Three-Dimensional Double Layers. *The Journal of Physical Chemistry C* 2014, **118**(32)**:** 18285–18290.

21. Largeot C, Portet C, Chmiola J, Taberna P-L, Gogotsi Y, Simon P. Relation between the Ion Size and Pore Size for an Electric Double-Layer Capacitor. *Journal of the American Chemical Society* 2008, **130**(9)**:** 2730-2731.

22. Zhong C, Deng Y, Hu W, Qiao J, Zhang L, Zhang J. A review of electrolyte materials and compositions for electrochemical supercapacitors. *Chemical Society Reviews* 2015, **44**(21)**:** 7484-7539.

23. Yang X, Cheng C, Wang Y, Qiu L, Li D. Liquid-Mediated Dense Integration of Graphene Materials for Compact Capacitive Energy Storage. *Science* 2013, **341**(6145)**:** 534-537.

24. Yang H, Kannappan S, Pandian AS, Jang J-H, Lee YS, Lu W. Graphene supercapacitor with both high power and energy density. *Nanotechnology* 2017, **28**(44)**:** 445401.

25. Kondrat S, Wu P, Qiao R, Kornyshev AA. Accelerating charging dynamics in subnanometre pores. *Nature Materials* 2014, **13**(4)**:** 387-393.

26. Masarapu C, Zeng HF, Hung KH, Wei B. Effect of Temperature on the Capacitance of Carbon Nanotube Supercapacitors. *ACS Nano* 2009, **3**(8)**:** 2199-2206.

27. Fletcher SI, Sillars FB, Carter RC, Cruden AJ, Mirzaeian M, Hudson NE*, et al.* The effects of temperature on the performance of electrochemical double layer capacitors. *J Power Sources* 2010, **195**(21)**:** 7484-7488.

28. Stoppa A, Zech O, Kunz W, Buchner R. The Conductivity of Imidazolium-Based Ionic Liquids from (−35 to 195) °C. A. Variation of Cation's Alkyl Chain. *Journal of Chemical & Engineering Data* 2010, **55**(5)**:** 1768-1773.

29. Kondrat S, Kornyshev AA. Superionic state in double-layer capacitors with nanoporous electrodes. *Journal of Physics: Condensed Matter* 2011, **23**(2)**:** 022201.

30. Futamura R, Iiyama T, Takasaki Y, Gogotsi Y, Biggs MJ, Salanne M*, et al.* Partial breaking of the Coulombic ordering of ionic liquids confined in carbon nanopores. *Nature Materials* 2017, **16:** 1225.

31. Merlet C, Rotenberg B, Madden PA, Taberna P-L, Simon P, Gogotsi Y*, et al.* On the molecular origin of supercapacitance in nanoporous carbon electrodes. *Nature Materials* 2012, **11**(4)**:** 306-310.

32. Sheberla D, Sun L, Blood-Forsythe MA, Er S, Wade CR, Brozek CK*, et al.* High Electrical Conductivity in Ni_3(2,3,6,7,10,11-hexaiminotriphenylene)$_2$, a Semiconducting Metal–

Organic Graphene Analogue. *Journal of the American Chemical Society* 2014, **136**(25)**:** 8859-8862.

33. Chaban VV, Voroshylova IV, Kalugin ON. A new force field model for the simulation of transport properties of imidazolium-based ionic liquids. *Physical Chemistry Chemical Physics* 2011, **13**(17)**:** 7910-7920.
34. Sun L, Liao B, Sheberla D, Kraemer D, Zhou J, Stach EA*, et al.* A Microporous and Naturally Nanostructured Thermoelectric Metal-Organic Framework with Ultralow Thermal Conductivity. *Joule* 2017, **1**(1)**:** 168-177.
35. Park J, Lee M, Feng D, Huang Z, Hinckley AC, Yakovenko A*, et al.* Stabilization of Hexaaminobenzene in a 2D Conductive Metal–Organic Framework for High Power Sodium Storage. *Journal of the American Chemical Society* 2018, **140**(32)**:** 10315-10323.
36. Nonoguchi Y, Sato D, Kawai T. Crystallinity-Dependent Thermoelectric Properties of a Two-Dimensional Coordination Polymer: Ni_3(2,3,6,7,10,11-hexaiminotriphenylene)$_2$. *Polymers* 2018, **10:** 962.
37. Izadi-Najafabadi A, Futaba DN, Iijima S, Hata K. Ion Diffusion and Electrochemical Capacitance in Aligned and Packed Single-Walled Carbon Nanotubes. *Journal of the American Chemical Society* 2010, **132**(51)**:** 18017-18019.
38. Eftekhari A. Supercapacitors utilising ionic liquids. *Energy Storage Materials* 2017, **9:** 47-69.
39. González A, Goikolea E, Barrena JA, Mysyk R. Review on supercapacitors: Technologies and materials. *Renewable and Sustainable Energy Reviews* 2016, **58:** 1189-1206.
40. Li P, Wang B. Recent Development and Application of Conductive MOFs. *Israel Journal of Chemistry* 2018, **58**(9-10)**:** 1010-1018.
41. Vatamanu J, Vatamanu M, Bedrov D. Non-Faradaic Energy Storage by Room Temperature Ionic Liquids in Nanoporous Electrodes. *ACS Nano* 2015, **9**(6)**:** 5999-6017.
42. Park J, Hinckley AC, Huang Z, Feng D, Yakovenko AA, Lee M*, et al.* Synthetic Routes for a 2D Semiconductive Copper Hexahydroxybenzene Metal–Organic Framework. *Journal of the American Chemical Society* 2018, **140**(44)**:** 14533-14537.
43. Kresse G, Furthmüller J. Efficiency of ab-initio total energy calculations for metals and semiconductors using a plane-wave basis set. *Computational Materials Science* 1996, **6**(1)**:** 15-50.
44. Rappe AK, Casewit CJ, Colwell KS, Goddard WA, Skiff WM. UFF, a full periodic table force field for molecular mechanics and molecular dynamics simulations. *Journal of the American Chemical Society* 1992, **114**(25)**:** 10024-10035.
45. Hess B, Kutzner C, van der Spoel D, Lindahl E. GROMACS 4: Algorithms for Highly Efficient, Load-Balanced, and Scalable Molecular Simulation. *Journal of Chemical Theory and Computation* 2008, **4**(3)**:** 435-447.
46. Bussi G, Donadio D, Parrinello M. Canonical sampling through velocity rescaling. *The Journal of Chemical Physics* 2007, **126**(1)**:** 014101.
47. Gingrich TR, Wilson M. On the Ewald summation of Gaussian charges for the simulation of

metallic surfaces. *Chemical Physics Letters* 2010, **500**(1)**:** 178-183.

48. Fang T, Konar A, Xing H, Jena D. Carrier statistics and quantum capacitance of graphene sheets and ribbons. *Applied Physics Letters* 2007, **91**(9)**:** 092109-092103.

49. Xia J, Chen F, Li J, Tao N. Measurement of the quantum capacitance of graphene. *Nature Nanotechnology* 2009, **4**(8)**:** 505-509.

50. Zhan C, Neal J, Wu J, Jiang D. Quantum Effects on the Capacitance of Graphene-Based Electrodes. *The Journal of Physical Chemistry C* 2015, **119**(39)**:** 22297-22303.

Acknowledgements

G.F., S.B., M.C., L.N., M.Y.C., T.Z.W., J.S.W., R.X.W., and J.M.F. acknowledge the funding support from the National Natural Science Foundation of China (51876072, 51836003) and Shenzhen Basic Research Project (JCYJ20170307171511292). S.B. and R.X.W. thank the financial support from China Scholarship Council. A.A.K. acknowledges the Leverhulme Trust for funding (RPG-2016-223) and HUST for the support of this project through the HUST Honorary Professorship and Imperial College for the support of this form of collaboration between the involved HUST and Imperial groups. M.D., H.B., and T.Y.C. thank the Army Research Office (W911NF-17-1-0174) for support. The computation is completed using Tianhe II supercomputer in National Supercomputing Center in Guangzhou.

Author contributions

G.F. and A.A.K. set the strategy of this project in consultation with M.D.; G.F. devised simulation approaches; G.F. and M.D. designed the experiment. S.B. performed major part of molecular dynamics simulations with participation of M.C., R.X.W. and J.M.F.; M.C. did all DFT calculations; H.B., L.N., M.Y.C., T.Z.W., J.S.W., and T.Y.C. carried out the experiment in which L.N. developed MOF synthesis procedures; G.F., S.B., M.C., L.N., M.Y.C. and A.A.K. analyzed the data and wrote the manuscript; G.F., S.B., A.A.K., M.C., H.B., and M.D. contributed to the discussion of results, editing and revising the paper.

Additional information

Supplementary information is available for this paper at ...

Competing interests

The authors declare no competing interests.

Figure 1

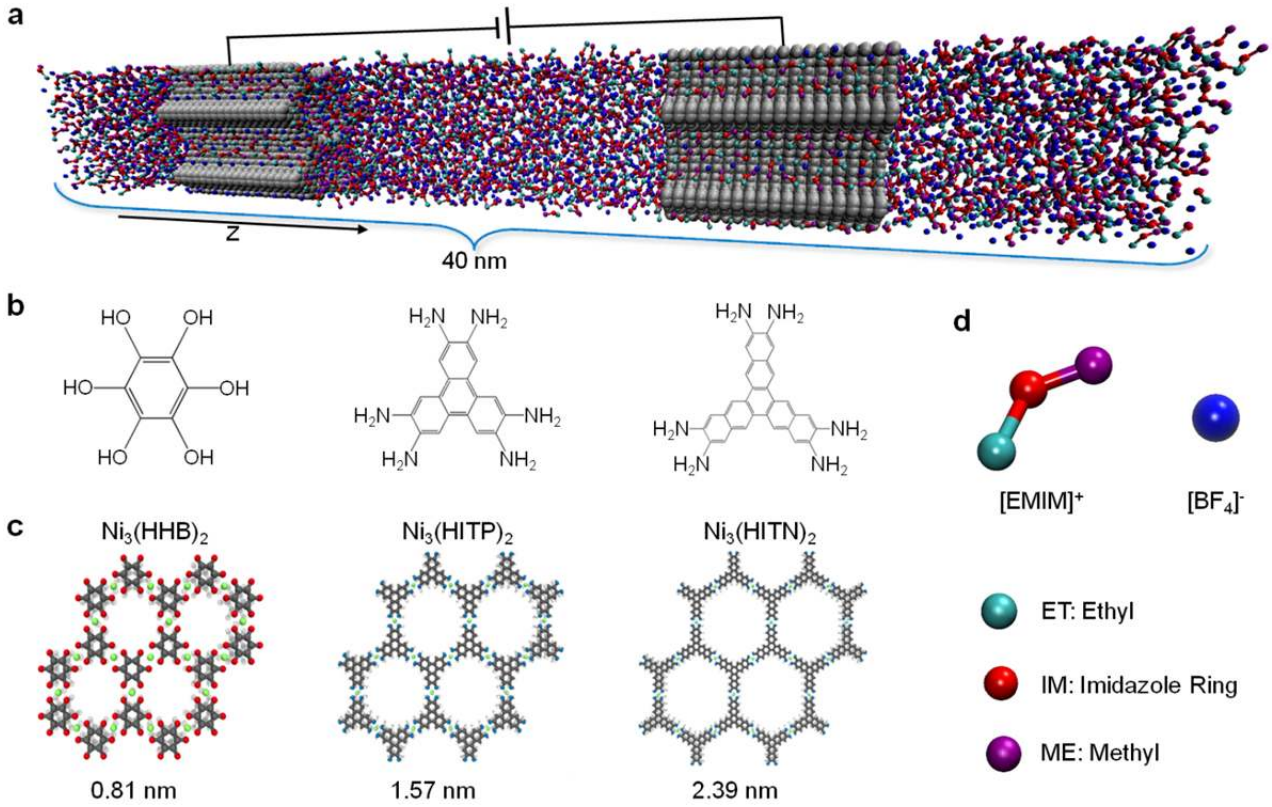

Fig. 1 | Schematics of MD simulation of MOF-based supercapacitors. a, A snapshot of the simulation system containing two identical MOF electrodes connected with RTIL reservoirs (periodically repeated in all three dimensions). Each electrode has stacks of eighteen 2D MOF sheets. **b,** Molecular structures of the linkers used for three studied MOFs. **c,** 2D honeycomb structures of MOF sheets studied. The numbers at the bottom indicate characteristic in-plane sizes of quasi-1D pores formed by the stacked MOF sheets (i.e., effective pore diameters). **d,** Coarse-grained model of RTIL [EMIM][BF_4]. Details for all three studied MOFs and simulation setup can be found in Supplementary Part 1 and Supplementary Tables 1-3.

Figure 2

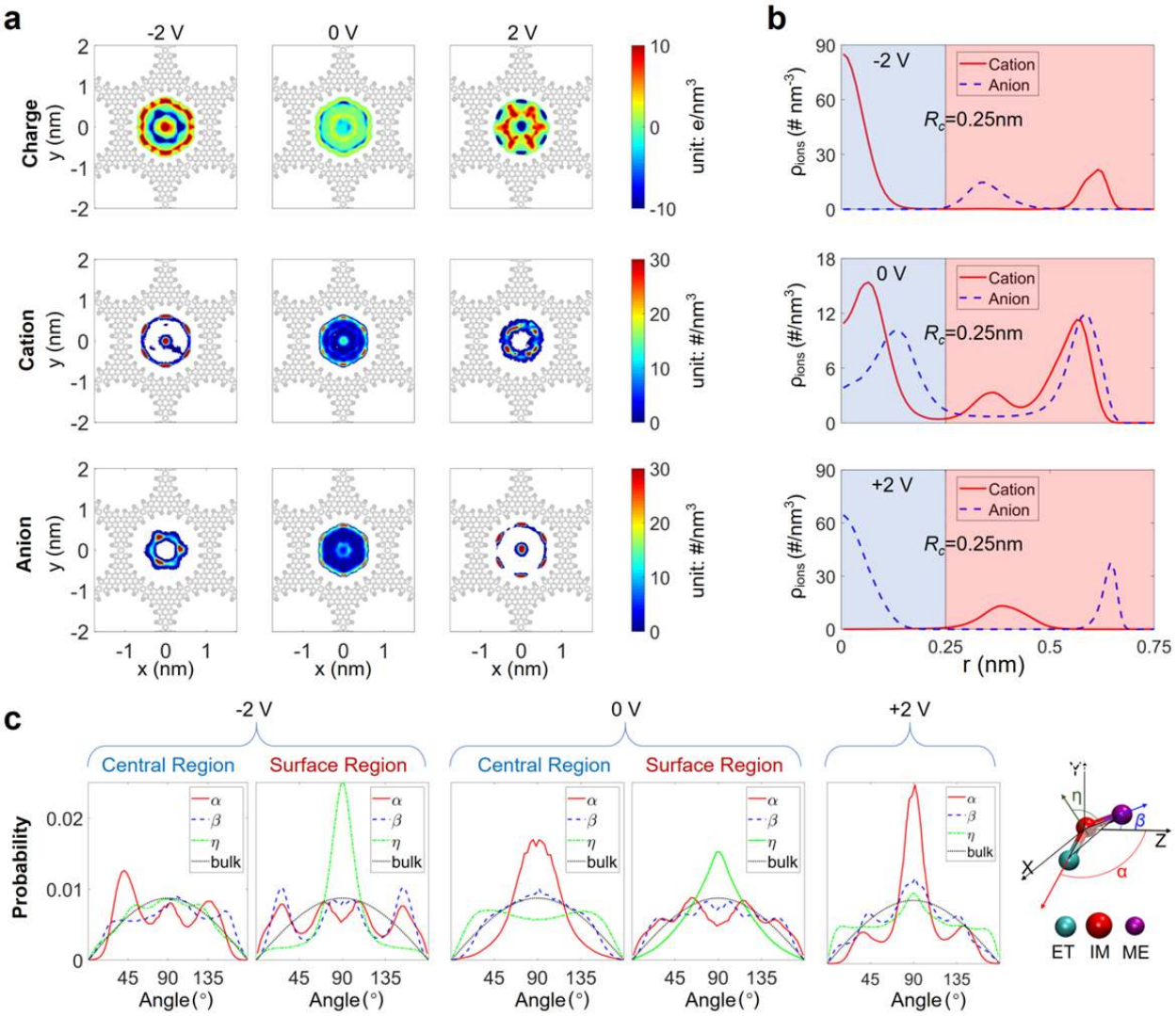

Fig. 2 | In-pore charge/ion density and orientation distributions. a, In-plane, 2D maps of charge and ion distributions of [EMIM][BF_4] inside a pore of a studied MOF. Each map is based on simulation data averaged along the pore axis (pore diameter is 1.57 nm). Columns correspond to three (indicated) electrode potentials (0 V means PZC, see the main text) and rows indicate 2D charge distributions (up row) and 2D number density distributions of cations (middle row) and anions (bottom row). For better visibility, results for neighboring pores are not displayed, and in the central pore the areas where no ions could access are shown in white. **b**, Radial ion distributions of ion inside pore. r = 0 stands for the pore centre. The light blue and red shaded areas, separated by a critical value of radial distance (R_c = 0.25 nm), represent the central and surface regions of the pore space. **c,** Angular distribution of cations located in central and surface regions of the MOF pore.

Figure 3

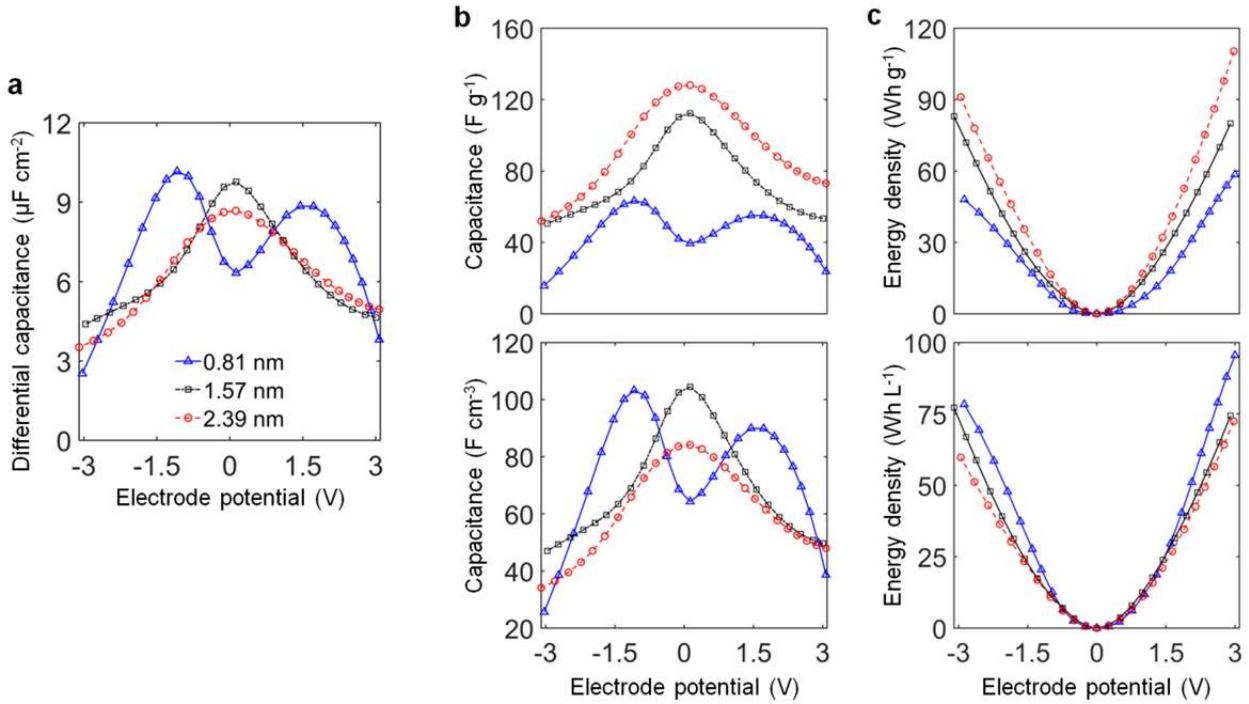

Fig. 3 | Capacitance and energy density. Voltage dependence of the capacitance of ionic-liquid-filled MOF electrode and the stored energy density. **a,** Differential capacitance per unit pore surface area. **b-c,** Gravimetric (**b**) and volumetric (**c**) capacitance and energy density of three studied MOFs. The energy density is calculated by $\mathrm{E}_{\mathrm{g/v}}(\varphi) = \int \varphi C_{\mathrm{g/v}}(\varphi) d\varphi$, where $C_{\mathrm{g/v}}$ is the gravimetric/volumetric capacitance.

Figure 4

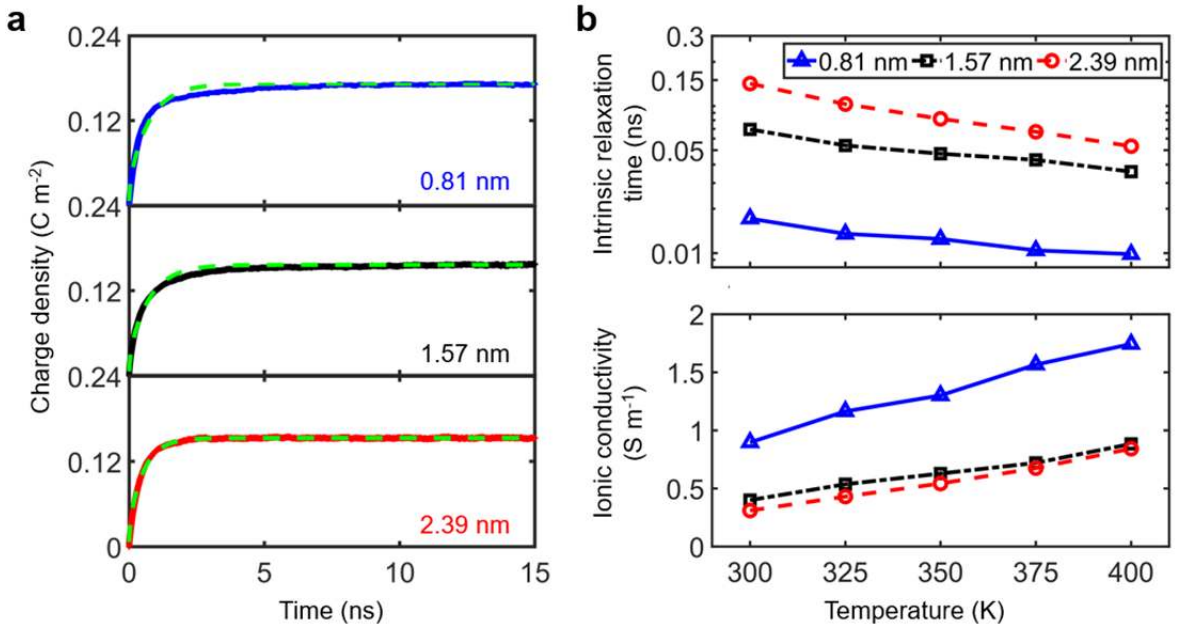

Fig. 4 | Charging process at nanoscale. a, Time evolution of charge density per unit surface area of the pore, after a cell voltage of 4 V was applied between two electrodes, shown for the positive electrode, for three MOFs of indicated pore sizes at 400 K. MD-obtained results are shown against the curves (green dashed lines) fitted by the transmission line model sketched in Supplementary Figure 12a. **b**, Intrinsic relaxation time (top panel, shown in logarithmic scale for better visibility) and the ionic conductivity (bottom panel) of RTILs in the MOF pores at different temperature.

Figure 5

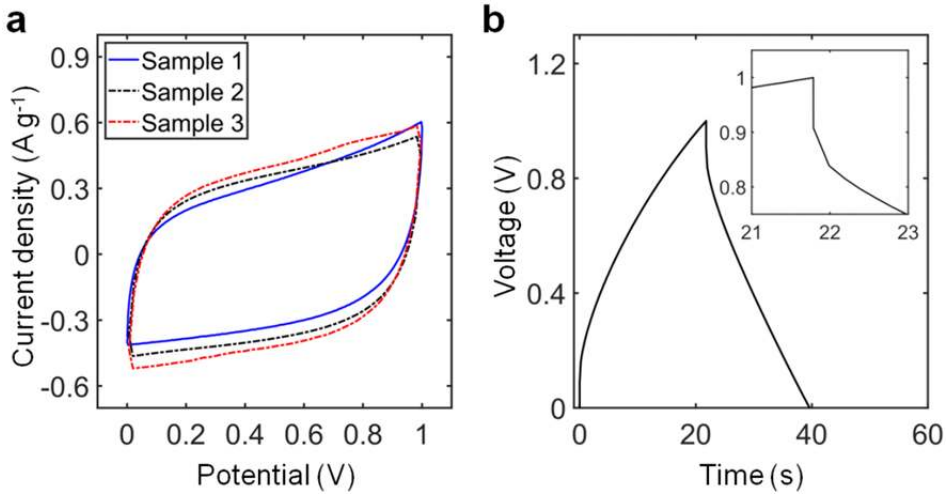

Fig. 5 | Capacitive measurement of $Ni_3(HITP)_2$ electrodes in a symmetrical supercapacitor cell. **a,** Cyclic voltammograms at a scan rate of 10 mV s^{-1}. Sample 1, 2, and 3 have specific surface areas of 556, 641, and 732 m^2 g^{-1}, respectively. **b,** Galvanostatic charge and discharge curve of two-electrode cells with pellet MOF $Ni_3(HITP)_2$ at a current density of 0.5 A g^{-1}. Inset enucleates how to determine the ESR from the potential drop at the beginning of a constant current discharge.

Figure 6

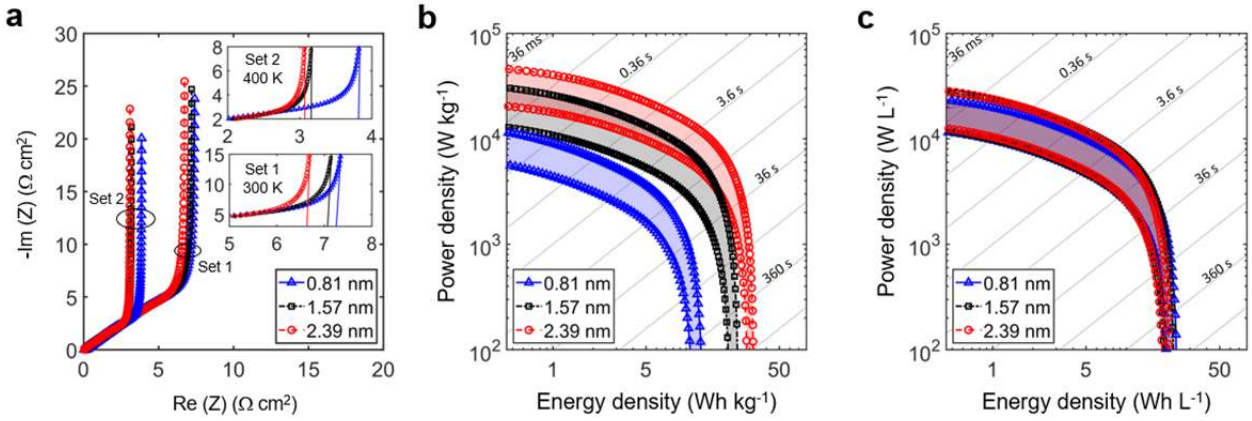

Fig. 6 | Capacitive performance predicted for practical cell-size supercapacitors. **a,** Nyquist plots for MOF-based supercapacitors at temperatures of 300 K (Set 1) and 400 K (Set 2). **b-c,** Gravimetric (**b**) and volumetric (**c**) Ragone plots for MOF-based supercapacitors from 300 to 400 K. Blue triangles, black squares, and red dots represent results for MOFs with the pore sizes of 0.81, 1.57, and 2.39 nm, respectively. Grey dotted lines in **b-c** indicate the lasting time that quantifies how long a supercapacitor can supply the power at an appointed power-energy point. The voltage between cathode and anode is 2.8 V.